Supersolid Phases of Bosonic Particles in a Bubble Trap

Matteo Ciardi [1,2,3,*] Fabio Cinti [1,3,4,†] Giuseppe Pellicane,[5–8,‡] and Santi Prestipino [9,§]

[1]*Dipartimento di Fisica e Astronomia, Università di Firenze, I-50019 Sesto Fiorentino (FI), Italy*
[2]*Institute for Theoretical Physics, TU Wien, Wiedner Hauptstraße 8-10/136, 1040 Vienna, Austria*
[3]*INFN, Sezione di Firenze, I-50019 Sesto Fiorentino (FI), Italy*
[4]*Department of Physics, University of Johannesburg, P.O. Box 524, Auckland Park 2006, South Africa*
[5]*Dipartimento di Scienze Biomediche, Odontoiatriche e delle Immagini Morfologiche e Funzionali,*
Università degli Studi di Messina, I-98125 Messina, Italy
[6]*CNR-IPCF, Viale F. Stagno d'Alcontres, 37-98158, Messina, Italy*
[7]*School of Chemistry and Physics, University of Kwazulu-Natal, 3209 Pietermaritzburg, South Africa*
[8]*National Institute of Theoretical and Computational Sciences (NIThECS), 3209 Pietermaritzburg, South Africa*
[9]*Dipartimento di Scienze Matematiche e Informatiche, Scienze Fisiche e Scienze della Terra,*
Università degli Studi di Messina, viale F. Stagno d'Alcontres 31, I-98166 Messina, Italy

Confinement can have a considerable effect on the behavior of particle systems and is therefore an effective way to discover new phenomena. A notable example is a system of identical bosons at low temperature under an external field mimicking an isotropic bubble trap, which constrains the particles to a portion of space close to a spherical surface. Using path integral Monte Carlo simulations, we examine the spatial structure and superfluid fraction in two emblematic cases. First, we look at soft-core bosons, finding the existence of supersolid cluster arrangements with polyhedral symmetry; we show how different numbers of clusters are stabilized depending on the trap radius and the particle mass, and we characterize the temperature behavior of the cluster phases. A detailed comparison with the behavior of classical soft-core particles is provided too. Then, we examine the case, of more immediate experimental interest, of a dipolar condensate on the sphere, demonstrating how a quasi-one-dimensional supersolid of clusters is formed on a great circle for realistic values of density and interaction parameters. Crucially, this supersolid phase is only slightly disturbed by gravity. We argue that the predicted phases can be revealed in magnetic traps with spherical-shell geometry, possibly even in a lab on Earth. Our results pave the way for future simulation studies of correlated quantum systems in curved geometries.

Computing the equilibrium properties of quantum many-body systems remains a main objective of contemporary physics. In this respect, ultracold atoms provide a framework where geometry and interactions can be tuned almost at will, allowing one to test fundamental many-body theories [1,2]. A system of atoms (loosely) confined to an ellipsoidal surface [3,4] represents a typology that only recently has started to be explored. To achieve this goal, a quantum gas is loaded into a shell trap, where atoms are subject to a quadrupolar field "dressed" by a radio frequency (rf) field [5–9]. In the limit of slow atomic motion in a strong magnetic field, the effective potentials of the internal states are the position-dependent eigenvalues of the Hamiltonian consisting of the bare potentials and the coupling term [10]. For atoms in the upper dressed state, resonance is reached at the surface of an ellipsoid. However, to let atoms explore the full surface, experiments must be performed in outer space [11–13] or adopt some gravity compensation mechanism [14,15]. Coherent and isotropic shells of atoms slowly expanding in microgravity can be generated too [16].

The realization of shell-shaped condensates has fueled a renewed interest in the problem of quantum particles in curved geometries [17], and particularly in the quantum phases that free and interacting bosons can exhibit. Several recent works have investigated Bose-Einstein condensation as well as the superfluid-to-normal fluid transition on a sphere [18–22], while others have studied the dynamics and thermodynamics of the condensate itself [23–26]. Most of these works have considered weakly interacting particles, although some have looked into the condensed phases arising from dipolar interactions [26–29].

While experiments have so far been performed in the same dilute limit, bubble traps open the exciting prospect of investigating the physics of strongly correlated quantum particles in curved spaces, with all the advantages brought by ultracold-atom setups. For example, ultracold atoms may serve as quantum simulators to test fundamental physics; therefore, studying the effects of curvature in a controlled environment can be of interest to other fields ranging from cosmology to biology [30,31]. Similarly, we

026001-1

can envisage the possibility to control the self-assembly of a many-body system through a convenient choice of the confining surface, i.e., of the shape of the ensuing geometric potential [17]. Equally important is to figure out experiments on curved many-body systems that could be accomplished on Earth, i.e., without the necessity of compensating gravity [32]. In this respect, the most awaited developments concern dipolar atoms [33], which have already been examined in flat space and harmonic traps [34,35] and are known to give rise to supersolid phases [36–39]. At the same time, it will be interesting to see whether the confined geometry of bubble traps can stabilize the supersolid phase in small systems of Rydberg-dressed atoms [40–44].

In this Letter, we use the path integral Monte Carlo (PIMC) simulation method to give a first glimpse of the equilibrium phases that can arise in a shell-trapped system of identical bosonic particles. In particular, we will provide the first compelling evidence of supersolid order for two distinct instances of the interaction potential. First, we look at the penetrable-sphere model as an example of soft-core potential and a paradigmatic interaction in condensed matter physics that gives rise to both superfluidity and clusterization [45–48]; for this interaction, we compare our results with various benchmarks. Then, we investigate the effects of a dipole-dipole interaction, more closely related to experiments, and we show, for a realistic choice of parameters, that a supersolid cluster phase indeed occurs in shell geometry. Remarkably, this supersolid is resistant to the gravity of Earth.

To keep contact with the experiments, we simulate spinless bosons in three-dimensional space under the constraint of an external potential analogous to that realized in the lab. For N particles with mass m, the Hamiltonian reads

$$H = \sum_{i=1}^{N} (-\lambda \nabla_{\mathbf{r}_i}^2 + u_{\text{ext}}(|\mathbf{r}_i|)) + \sum_{i<j} v_{\text{int}}(\mathbf{r}_i - \mathbf{r}_j), \quad (1)$$

where $\mathbf{r}_i$ is the position of the ith particle, $\lambda = \hbar^2/2m$, v_{int} is the (possibly anisotropic) interaction potential, and

$$u_{\text{ext}}(d) = (u_0/\Omega)\sqrt{(d^2 - \Delta)^2/4 + \Omega^2} - u_0 \quad (2)$$

is the external potential appropriate to a spherically symmetric bubble trap [24] centered at the origin. In Eq. (2), Δ and Ω are square-length parameters related to the detuning and Rabi frequency of the rf field, respectively, while u_0 characterizes the harmonic trap prior to dressing. The potential (2) interpolates between the filled sphere and the spherical shell [see Fig. 1(g)]. In the thin-shell limit, u_{ext} becomes harmonic around the minimum at $\sqrt{\Delta}$, which thus defines the radius R of the reference sphere. As R increases, the potential minimum gets more and more pronounced,
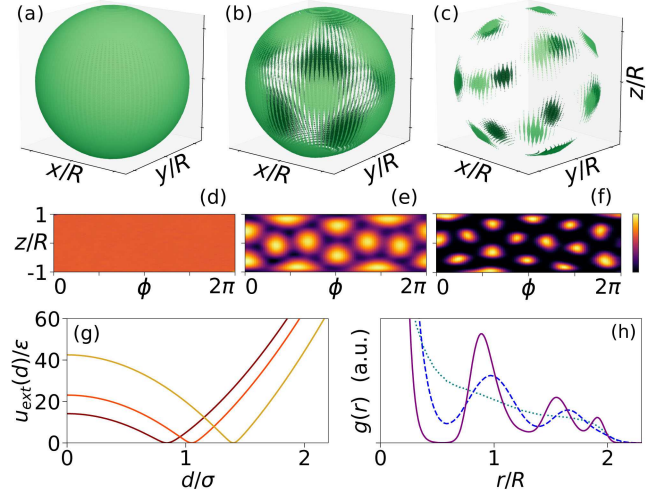

FIG. 1. Soft-core bosons in an isotropic bubble trap. (a)–(c) Particle density for $N = 120$, $T = 0.125$, $R = 1.4$, $u_0 = 2$, $\Omega = 0.0441$, and $\lambda = 0.5$ (a), 0.16 (b), 0.01 (c). The size of the points is proportional to the density averaged along the radial direction, and the shading is a guide for the eye: Brighter points are closer to the observer. (d)–(f) Area-preserving projections of the densities in (a)–(c). Brighter colors indicate a larger density (log scale). (g) External potential (2) for $u_0 = 2$, $\Omega = 0.0441$, and $R = 0.84$ (brown), 1.05 (red), and 1.4 (gold). (h) Pair distribution function for the same parameters in (a)–(c): $\lambda = 0.5$ (blue dotted line), 0.16 (blue dashed line), 0.01 (purple solid line).

until particles become effectively confined to a spherical surface.

In our PIMC simulations [49], we employ the worm algorithm [50] to sample the equilibrium statistics of bosons at finite temperature and estimate the superfluid fraction, f_s [51]. To deal with the strong spatial constraint due to (2), we introduce a biased version of the PIMC method [51]. We also perform classical Monte Carlo (MC) and molecular dynamics (MD) simulations to probe the classical limit in the soft-core case.

We begin by considering bosons interacting through the soft-core potential:

$$v_{\text{int}}(\mathbf{r}) = \epsilon \theta(\sigma - r), \quad (3)$$

where $\epsilon > 0$, and σ is the core diameter. In the discussion of the soft-core model, ϵ and σ are taken as units of energy and length, respectively; temperatures are expressed in units of ϵ/k_B. Because of the peculiar nature of the repulsion, at high density particles are gathered in droplets or clusters [77]. Employing mean-field theory at $T = 0$, the authors of Ref. [78] explored various possible arrangements of clusters on the sphere, finding the configuration of lowest enthalpy as a function of the radius. The evidence of supersolid phases is, however, not conclusive: Condensation of clusters is assumed, not derived, while there is no guarantee that the true ground state has been identified. Using, for the first time, *ab initio* PIMC simulations, we provide for the

same interaction (3) conclusive evidence of supersolid order. Moreover, we show how the supersolid withstands finite temperature in a realistic bubble trap, i.e., beyond a purely two-dimensional setup.

First, we investigate the behavior of the system at a temperature $T \ll 1$, choosing $\Omega = 0.0441$ (an arbitrary value much smaller than Δ; see below). In Figs. 1(a)–1(f), we give a graphical account of the structures found for decreasing λ at $T = 0.125$, which are indicative of a superfluid-supersolid-insulator "transition," similar to what occurs on a plane [79]. Specifically, we perform a size scaling analysis of f_s at fixed $N/(4\pi R^2) = 4.87$ for two strengths of the trap potential to see how the system approaches the planar limit. On a plane, the phases were characterized in terms of the dimensionless interaction strength $\alpha = m\rho\sigma^4\epsilon/\hbar^2 = \rho\sigma^4\epsilon/(2\lambda)$ (for a number density $\rho = 4.4$), finding that the superfluid-supersolid transition occurs at $\alpha \approx 13$, whereas the system becomes insulating at $\alpha \approx 22$ [79]. In both two and three dimensions, the former transition is marked by a jump in f_s [45]. Our results are reported in Fig. 2. In the strongly confined case ($u_0 = 50$, top panel), the planar behavior is already recovered for $N = 120$ particles, while for smaller sizes we find a smooth crossover. For a weaker external potential ($u_0 = 2$, bottom panel), the transition to supersolid is milder and shifted toward higher α values; moreover, convergence to the planar limit is much slower. In both cases, the system is a density wave at large α; as α is reduced, quantum fluctuations increase, eventually leading to a disruption of polyhedral order which is faster when more freedom is given to particles in the radial direction, i.e., for $u_0 = 2$. The same sequence of transitions is reflected in the shape of the pair distribution function $g(r)$ [see Fig. 1(h) and [51]]. As

long as $f_s > 0$, $g(r)$ is nonzero at any distance, which is consistent with a condensate wave function being nonzero everywhere on the sphere. Instead, in a normal solid near zero temperature, $g(r)$ would ideally be zero in the interstitial region between two successive shells of neighbors. The deviations from this behavior at moderate to large distances are a temperature effect, ultimately due to the finite extension of the clusters.

Next, we fix the number N of particles (120) and the temperature T (0.5), and set $u_0 = 2$ and $\Omega = 0.0441$ [we require $\Omega \ll 1$, so as to have $u_{\text{ext}}(0) \approx \Delta/\Omega \gg 1$ for $R \approx 1$]. We collect in a diagram the equilibrium arrangements for various λ and R [Fig. 3(a)]. On account of the f_s value and the evidence or not of polyhedral order, we can reasonably distinguish between superfluid, supersolid, and normal-solid states. Throughout the "solid" regions, the number N_c of clusters may vary, but clusters are invariably found at the vertices of a regular or semiregular polyhedron: for example, an octahedron for $N_c = 6$, a square antiprism for $N_c = 8$, and an icosahedron for $N_c = 12$ [51]. For some (λ, R) pairs, the cluster structure agrees with those predicted in [78] (for example, the icosahedral structure at $\lambda = 0.16$ and $R = 1.4$). However, for several other pairs, the equilibrium configuration is a novel cluster phase not seen before. Moreover, contrary to the mean-field prediction, we see that decreasing λ at fixed R leads to
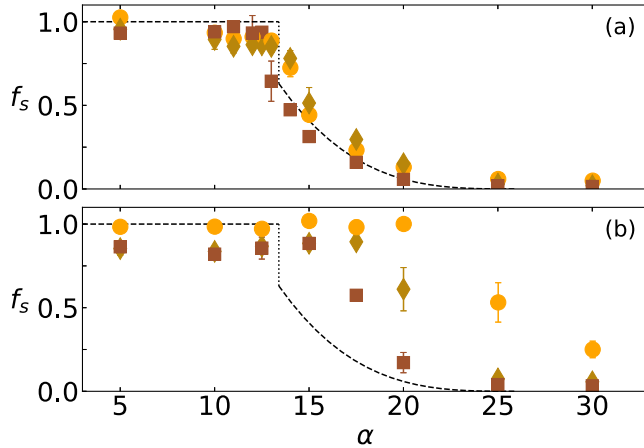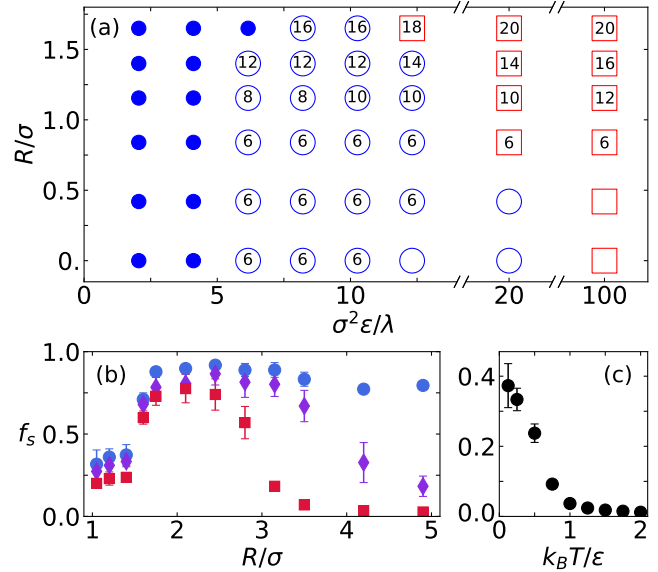

FIG. 2. Superfluid fraction across the superfluid-supersolid-insulator transition plotted as a function of α for $T = 0.125$ [the ρ entering the expression of α is $N/(4\pi R^2)$]. (a) $u_0 = 50$. (b) $u_0 = 2$. Different symbols correspond to different system sizes: $N = 40$ and $R = 0.808$ (circles), $N = 80$ and $R = 1.143$ (diamonds), $N = 120$ and $R = 1.4$ (squares). The dashed lines refer to the planar limit [80].

FIG. 3. (a) A diagram showing for $N = 120$ and $T = 0.5$ the number N_c of clusters as a function of λ^{-1} and R. The blue dots are state points where the system is superfluid. Open circles and squares mark supersolid and normal-solid states, respectively. When λ and R are both small, N_c depends on the initial conditions (see more in [51]); therefore, no number is printed in the symbol. (b) Superfluid fraction f_s plotted as a function of R at fixed $\lambda = 0.16$ and $u_0 = 50$ for $T = 0.5$ (red squares), 0.25 (purple diamonds), and 0.125 (blue circles). (c) T dependence of f_s for $R = 1.4$ and $\lambda = 0.16$.

transitions between equilibrium configurations with different numbers of clusters. As we increase the radius, the supersolid region shrinks, while the number of clusters grows. At large radii, the particles assemble in smaller clusters, making it more difficult for the system to sustain superfluidity; eventually, above a certain R the system is so dilute that clusters are washed away for every λ.

In the $T \to 0$ limit, the superfluid phase is stable at all large radii. Upon heating, similar to flat space, a superfluid-to-normal-fluid transition eventually occurs. This is illustrated for $\lambda = 0.16$ in Fig. 3(b), where we plot the superfluid fraction as a function of R at different temperatures. As T goes up, f_s is gradually reduced until it vanishes, starting from larger R values. At high enough temperatures, f_s is also depleted for the supersolid, as we show in Fig. 3(c) for $R = 1.4$ and $\lambda = 0.16$: Interestingly, however, polyhedral order is preserved throughout the range of temperatures.

When $\lambda \to 0$, the number of clusters approaches a value dependent on R; this regime corresponds to the classical limit, regardless of R and $T > 0$. To make sure that this is indeed the case, we have considered the classical counterpart of the quantum problem. The first observation of cluster phases in classical particles on a sphere goes back to Ref. [81], where density-functional-theory calculations are presented. Here, to keep the same level of accuracy of the quantum treatment, we carry out extensive MC and MD simulations of classical soft-core particles, using the same parameters of the quantum simulations. The results expressed in terms of the number and final arrangement of clusters are reported in [51] for various R values. Except for small radii, where the uncertainty in N_c is large, the aggregates formed by quantum particles have a comparatively smaller number of clusters. This is an effect of quantum delocalization, which causes the effective diameter of bosons to be larger than σ.

We now move to examine the behavior of dipolar bosons in the thin-shell limit. As is common in experiments, we assume atoms to be polarized along $\hat{\mathbf{z}}$. We work with a number density on the sphere of about $4 \ \mu\text{m}^{-2}$, of the same order as that used in experimental realizations [11]. The (anisotropic) interaction potential reads

$$v_{\text{int}}(\mathbf{r}) = v_{\text{HS}}(r) + \frac{\mu_0 d_m^2}{4\pi} \frac{1 - 3\cos^2\theta}{r^3}, \qquad (4)$$

where μ_0 is the vacuum permeability, $d_m = 9.93\mu_B$ is the magnitude of the dipole moment of a ^{164}Dy atom, μ_B is the Bohr magneton, and $\cos\theta = \hat{\mathbf{r}} \cdot \hat{\mathbf{z}}$ [82]. Finally, $v_{\text{HS}}(r)$ is the hard-sphere potential with core diameter equal to the scattering length a [51].

We simulate the system for various a, considering values up to $10^3 a_0$, with a_0 the Bohr radius, thus much smaller than the sphere radius taken to be $R = 2.6 \ \mu\text{m}$ (or $R \approx 50 \times 10^3 a_0$). Our results for $N = 360$ and $T = 1$ nK are illustrated in Fig. 4. As is clear from Eq. (4), particles
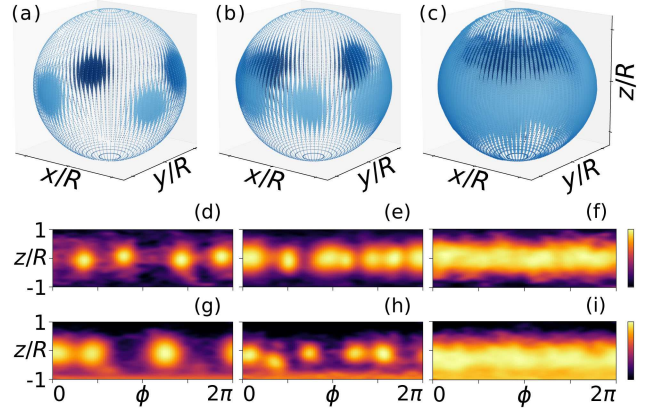

FIG. 4. Dipolar atoms on a sphere. (a)–(c) Particle density for $N = 360, T = 1$ nK, and $R = 2.6 \ \mu\text{m}$, at $a/a_0 = 5$ (a), $a/a_0 = 50$ (b), and $a/a_0 = 350$ (c). The density increases with the size of the points, while colors are a guide for the eye. (d)–(f) Area-preserving projections of the densities in (a)–(c). (g)–(i) Effect of gravity. Brighter colors indicate larger values of the density (log scale).

attract each other along the z direction and repel each other along x and y. As long as a is much smaller than R, particles move away from the poles of the sphere and bunch together around the equator. Indeed, up to $a \approx 150a_0$, particles form clusters lined up along the equator, as seen in Figs. 4(a) and 4(b). At variance with what is observed for dipolar clusters in trapped Euclidean geometries [36], the cluster phase on the sphere excludes zigzag configurations: In Figs. 4(a) and 4(b), clusters remain on the equator due to the lack of a significant repulsion along z that could counteract the mutual attraction. Unless a is very small, the superfluid fraction for rotations around z is finite and significantly larger than f_s for rotations around x and y, thus qualifying this state as supersolid [Fig. 5(a)] [83]. For
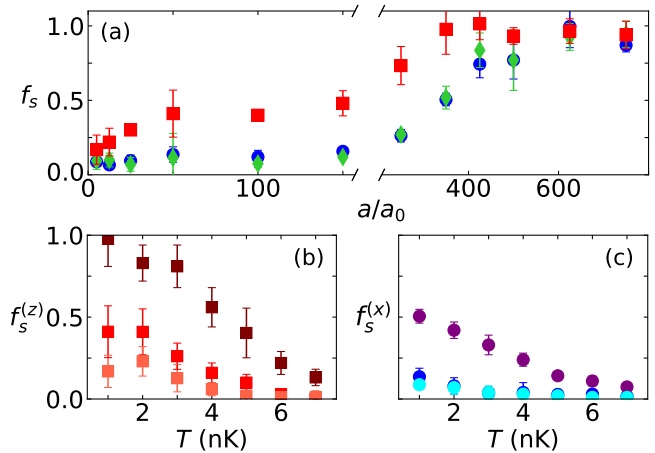

FIG. 5. (a) Superfluid fractions $f_s^{(x)}$ (blue circles), $f_s^{(y)}$ (green diamonds), and $f_s^{(z)}$ (red squares) as a function of a. (b),(c) Thermal behavior of $f_s^{(z)}$ and $f_s^{(x)}$, for $a/a_0 = 5$ (pink and light blue), 50 (red and blue), and 350 (brown and purple).

larger a, due to the increased particle exclusion, clusters grow in size and merge together forming a ribbon wrapped around the sphere; see Figs. 4(c) and 4(f). This specific configuration is consistent with the density profile seen in [26,27]. Beyond $a \approx 200a_0$, the ribbon is homogeneous; however, between $a = 150a_0$ and $a = 200a_0$, there is a wide crossover region where the clusters are still present as azimuthal density modulations. The modulated-to-unmodulated transition is shifted to slightly larger a compared to other trapped geometries (see, e.g., [85] and references cited therein) because of the enhanced stability of spherically confined clusters. The superfluid fraction along z is still significantly larger than in the other directions. Finally, for very large values of $a > 500a_0$, a homogeneous superfluid state emerges, similar to the one shown in Figs. 1(a) and 1(d). Simulations at different values of N but fixed density show no significant scaling, a strong indication that the same supersolid phase persists at larger numbers of particles, up to experimental values. The temperature analysis indicates that the supersolid behaves differently from the superfluid ribbon [see Figs. 5(b) and 5(c)]. In the former case, $f_s^{(z)}$ remains nonzero up to ≈ 5 nK due to a nonzero superfluid signal of the system around z. As for $f_s^{(x)}$, the signal is smaller and substantially constant as a result of the thickness of the supersolid in the latitudinal direction. Instead, the ribbon remains superfluid up to much higher temperatures, while keeping its anisotropic character for all T.

Figures 4(g)–4(i) depict simulations carried out by including the effect of gravity on ^{164}Dy atoms. Interestingly, for small enough a the atoms still form a ring of clusters perpendicular to z, although their center of mass is no longer at $z = 0$, but slightly shifted downward. For larger values of a, even though part of the atoms are found near the south pole, a shifted superfluid ribbon is still evident. This is to be contrasted with what happens when we remove the dipolar component of the interaction, but still keep the hard-core repulsion: In this case, all particles are pushed by gravity to the bottom of the trap [51].

To conclude, we have investigated the equilibrium phases of identical bosons in a shell trap. As the bubble expands, the system switches from three to two dimensional in a continuous fashion. In this peculiar setting, the PIMC algorithm needs an *ad hoc* modification that we have discussed at length in [51]. With this tool at hand, we have considered two species of bosons, i.e., soft-core atoms and dipolar atoms, providing evidence at small nonzero temperature of two unconventional supersolid behaviors. We have argued that the realization of these phases is within reach of present-day technology. Very significantly, we have shown that the dipolar supersolid on the sphere is robust to the effects of gravity. This surprising result indicates that it could be probed experimentally even without sending the apparatus to space. More generally, the ideas underlying our original implementation of the PIMC algorithm on the sphere can profitably be replicated for other curved surfaces, allowing us to gain insight into the peculiarities of bosons in spaces where the geometric potential is nonzero (see more in the last section of [51]).

In this Letter, we have focused on demonstrating the existence of a supersolid phase on the sphere. Using the same numerical techniques, it would be also possible to investigate the nature of the superfluid phase on the sphere, e.g., Berezinskii-Kosterlitz-Thouless behavior or reentrant effects [85,86]. Our work might also be relevant to super-solid phases in the crust of neutron stars [87]. The dynamical properties of shell-trapped bosons are another open problem and an active area of research [88]. For example, it would be interesting to see whether the super-fluid ribbon in Figs. 4(c) and 4(f) can support persistent currents in the same way as does a superfluid ring [89–91].

[*]matteo.ciardi@tuwien.ac.at
[†]fabio.cinti@unifi.it
[‡]giuseppe.pellicane@unime.it
[§]sprestipino@unime.it

[1] I. Bloch, J. Dalibard, and W. Zwerger, Many-body physics with ultracold gases, Rev. Mod. Phys. **80**, 885 (2008).

[2] I. Bloch, J. Dalibard, and S. Nascimbène, Quantum simulations with ultracold quantum gases, Nat. Phys. **8**, 267 (2012).

[3] B. M. Garraway and H. Perrin, Recent developments in trapping and manipulation of atoms with adiabatic potentials, J. Phys. B **49**, 172001 (2016).

[4] H. Perrin and B. M. Garraway, Trapping atoms with radio frequency adiabatic potentials, in *Advances in Atomic, Molecular, and Optical Physics* (Elsevier, New York, 2017), pp. 181–262.

[5] O. Zobay and B. M. Garraway, Two-dimensional atom trapping in field-induced adiabatic potentials, Phys. Rev. Lett. **86**, 1195 (2001).

[6] O. Zobay and B. M. Garraway, Atom trapping and two-dimensional Bose-Einstein condensates in field-induced adiabatic potentials, Phys. Rev. A **69**, 023605 (2004).

[7] Y. Colombe, E. Knyazchyan, O. Morizot, B. Mercier, V. Lorent, and H. Perrin, Ultracold atoms confined in rf-induced two-dimensional trapping potentials, Europhys. Lett. **67**, 593 (2004).

[8] O. Morizot, C. L. G. Alzar, P.-E. Pottie, V. Lorent, and H. Perrin, Trapping and cooling of rf-dressed atoms in a quadrupole magnetic field, J. Phys. B **40**, 4013 (2007).

[9] T. L. Harte, E. Bentine, K. Luksch, A. J. Barker, D. Trypogeorgos, B. Yuen, and C. J. Foot, Ultracold atoms

in multiple radio-frequency dressed adiabatic potentials, Phys. Rev. A **97**, 013616 (2018).

[10] A. Messiah, *Quantum Mechanics*, Dover Books on Physics (Dover Publications, Newburyport, 2014).

[11] N. Lundblad, R. A. Carollo, C. Lannert, M. J. Gold, X. Jiang, D. Paseltiner, N. Sergay, and D. C. Aveline, Shell potentials for microgravity Bose-Einstein condensates, npj Microgravity **5**, 30 (2019).

[12] D. C. Aveline, J. R. Williams, E. R. Elliott, C. Dutenhoffer, J. R. Kellogg, J. M. Kohel, N. E. Lay, K. Oudrhiri, R. F. Shotwell, N. Yu, and R. J. Thompson, Observation of Bose-Einstein condensates in an Earth-orbiting research lab, Nature (London) **582**, 193 (2020).

[13] R. A. Carollo, D. C. Aveline, B. Rhyno, S. Vishveshwara, C. Lannert, J. D. Murphree, E. R. Elliott, J. R. Williams, R. J. Thompson, and N. Lundblad, Observation of ultracold atomic bubbles in orbital microgravity, Nature (London) **606**, 281 (2022).

[14] Y. Guo, E. M. Gutierrez, D. Rey, T. Badr, A. Perrin, L. Longchambon, V. S. Bagnato, H. Perrin, and R. Dubessy, Expansion of a quantum gas in a shell trap, New J. Phys. **24**, 093040 (2022).

[15] F. Jia, Z. Huang, L. Qiu, R. Zhou, Y. Yan, and D. Wang, Expansion dynamics of a shell-shaped Bose-Einstein condensate, Phys. Rev. Lett. **129**, 243402 (2022).

[16] M. Meister, A. Roura, E. M. Rasel, and W. P. Schleich, The space atom laser: An isotropic source for ultra-cold atoms in microgravity, New J. Phys. **21**, 013039 (2019).

[17] N. S. Móller, F. E. A. dos Santos, V. S. Bagnato, and A. Pelster, Bose-Einstein condensation on curved manifolds, New J. Phys. **22**, 063059 (2020).

[18] A. Tononi and L. Salasnich, Bose-Einstein condensation on the surface of a sphere, Phys. Rev. Lett. **123**, 160403 (2019).

[19] S. J. Bereta, L. Madeira, V. S. Bagnato, and M. A. Caracanhas, Bose-Einstein condensation in spherically symmetric traps, Am. J. Phys. **87**, 924 (2019).

[20] A. Tononi, F. Cinti, and L. Salasnich, Quantum bubbles in microgravity, Phys. Rev. Lett. **125**, 010402 (2020).

[21] A. Tononi, A. Pelster, and L. Salasnich, Topological super-fluid transition in bubble-trapped condensates, Phys. Rev. Res. **4**, 013122 (2022).

[22] C. Lannert, T.-C. Wei, and S. Vishveshwara, Dynamics of condensate shells: Collective modes and expansion, Phys. Rev. A **75**, 013611 (2007).

[23] K. Padavić, K. Sun, C. Lannert, and S. Vishveshwara, Physics of hollow Bose-Einstein condensates, Europhys. Lett. **120**, 20004 (2018).

[24] K. Sun, K. Padavić, F. Yang, S. Vishveshwara, and C. Lannert, Static and dynamic properties of shell-shaped condensates, Phys. Rev. A **98**, 013609 (2018).

[25] B. Rhyno, N. Lundblad, D. C. Aveline, C. Lannert, and S. Vishveshwara, Thermodynamics in expanding shell-shaped Bose-Einstein condensates, Phys. Rev. A **104**, 063310 (2021).

[26] P. C. Diniz, E. A. B. Oliveira, A. R. P. Lima, and E. A. L. Henn, Ground state and collective excitations of a dipolar Bose-Einstein condensate in a bubble trap, Sci. Rep. **10**, 4831 (2020).

[27] S. K. Adhikari, Dipolar Bose-Einstein condensate in a ring or in a shell, Phys. Rev. A **85**, 053631 (2012).

[28] F. Cinti and M. Boninsegni, Classical and quantum filaments in the ground state of trapped dipolar Bose gases, Phys. Rev. A **96**, 013627 (2017).

[29] M. Arazo, R. Mayol, and M. Guilleumas, Shell-shaped condensates with gravitational sag: Contact and dipolar interactions, New J. Phys. **23**, 113040 (2021).

[30] S. Eckel, A. Kumar, T. Jacobson, I. B. Spielman, and G. K. Campbell, A rapidly expanding Bose-Einstein condensate: An expanding universe in the lab, Phys. Rev. X **8**, 021021 (2018).

[31] M. F. Hagan and G. M. Grason, Equilibrium mechanisms of self-limiting assembly, Rev. Mod. Phys. **93**, 025008 (2021).

[32] N. Lundblad, D. C. Aveline, A. Balaž, E. Bentine, N. P. Bigelow, P. Boegel, M. A. Efremov, N. Gaaloul, M. Meister, M. Olshanii, C. A. R. S. de Melo, A. Tononi, S. Vishveshwara, A. C. White, A. Wolf, and B. M. Garraway, Perspective on quantum bubbles in microgravity, Quantum Sci. Technol. **8**, 024003 (2023).

[33] T. Lahaye, C. Menotti, L. Santos, M. Lewenstein, and T. Pfau, The physics of dipolar bosonic quantum gases, Rep. Prog. Phys. **72**, 126401 (2009).

[34] G. Biagioni, N. Antolini, A. Alaña, M. Modugno, A. Fioretti, C. Gabbanini, L. Tanzi, and G. Modugno, Dimensional crossover in the superfluid-supersolid quantum phase transition, Phys. Rev. X **12**, 021019 (2022).

[35] L. Chomaz, I. Ferrier-Barbut, F. Ferlaino, B. Laburthe-Tolra, B. L. Lev, and T. Pfau, Dipolar physics: A review of experiments with magnetic quantum gases., Rep. Prog. Phys. **86**, 026401 (2023).

[36] M. A. Norcia, C. Politi, L. Klaus, E. Poli, M. Sohmen, M. J. Mark, R. N. Bisset, L. Santos, and F. Ferlaino, Two-dimensional supersolidity in a dipolar quantum gas, Nature (London) **596**, 357 (2021).

[37] L. Tanzi, E. Lucioni, F. Famà, J. Catani, A. Fioretti, C. Gabbanini, R. N. Bisset, L. Santos, and G. Modugno, Observation of a dipolar quantum gas with metastable supersolid properties, Phys. Rev. Lett. **122**, 130405 (2019).

[38] L. Chomaz, D. Petter, P. Ilzhöfer, G. Natale, A. Trautmann, C. Politi, G. Durastante, R. M. W. van Bijnen, A. Patscheider, M. Sohmen, M. J. Mark, and F. Ferlaino, Long-lived and transient supersolid behaviors in dipolar quantum gases, Phys. Rev. X **9**, 021012 (2019).

[39] F. Böttcher, J.-N. Schmidt, M. Wenzel, J. Hertkorn, M. Guo, T. Langen, and T. Pfau, Transient supersolid properties in an array of dipolar quantum droplets, Phys. Rev. X **9**, 011051 (2019).

[40] A. Browaeys and T. Lahaye, Many-body physics with individually controlled Rydberg atoms, Nat. Phys. **16**, 132 (2020).

[41] N. Henkel, R. Nath, and T. Pohl, Three-dimensional roton excitations and supersolid formation in Rydberg-excited Bose-Einstein condensates, Phys. Rev. Lett. **104**, 195302 (2010).

[42] G. Pupillo, A. Micheli, M. Boninsegni, I. Lesanovsky, and P. Zoller, Strongly correlated gases of Rydberg-dressed atoms: Quantum and classical dynamics, Phys. Rev. Lett. **104**, 223002 (2010).

[43] F. Cinti, P. Jain, M. Boninsegni, A. Micheli, P. Zoller, and G. Pupillo, Supersolid droplet crystal in a dipole-blockaded gas, Phys. Rev. Lett. **105,** 135301 (2010).

[44] J. B. Balewski, A. T. Krupp, A. Gaj, S. Hofferberth, R. Löw, and T. Pfau, Rydberg dressing: Understanding of collective many-body effects and implications for experiments, New J. Phys. **16,** 063012 (2014).

[45] F. Ancilotto, M. Rossi, and F. Toigo, Supersolid structure and excitation spectrum of soft-core bosons in three dimensions, Phys. Rev. A **88,** 033618 (2013).

[46] F. Cinti, T. Macrì, W. Lechner, G. Pupillo, and T. Pohl, Defect-induced supersolidity with soft-core bosons, Nat. Commun. **5,** 3235 (2014).

[47] M. Kunimi and Y. Kato, Mean-field and stability analyses of two-dimensional flowing soft-core bosons modeling a supersolid, Phys. Rev. B **86,** 060510(R) (2012).

[48] S. Prestipino, A. Sergi, and E. Bruno, Freezing of soft-core bosons at zero temperature: A variational theory, Phys. Rev. B **98,** 104104 (2018).

[49] D. M. Ceperley, Path integrals in the theory of condensed helium, Rev. Mod. Phys. **67,** 279 (1995).

[50] M. Boninsegni, Nikolay Prokof'ev, and B. Svistunov, Worm algorithm for continuous-space path integral Monte Carlo simulations, Phys. Rev. Lett. **96,** 070601 (2006).

[51] See Supplemental Material at http://link.aps.org/supplemental/10.1103/PhysRevLett.132.026001 which cites references [52–76], for additional information on the techniques used and results.

[52] R. Feynman, A. Hibbs, and D. Styer, *Quantum Mechanics and Path Integrals*, Dover Books on Physics (Dover Publications, New York, 2010).

[53] M. Boninsegni, Permutation sampling in path integral Monte Carlo, J. Low Temp. Phys. **141,** 27 (2005).

[54] J. Cao and B. J. Berne, A new quantum propagator for hard sphere and cavity systems, J. Chem. Phys. **97,** 2382 (1992).

[55] S. Pilati, S. Giorgini, and N. Prokof'ev, Critical temperature of interacting Bose gases in two and three dimensions, Phys. Rev. Lett. **100,** 140405 (2008).

[56] H. Saito, Path-integral Monte Carlo study on a droplet of a dipolar Bose-Einstein condensate stabilized by quantum fluctuation, J. Phys. Soc. Jpn. **85,** 053001 (2016).

[57] S. A. Chin, Symplectic integrators from composite operator factorizations, Phys. Lett. A **226,** 344 (1997).

[58] M. Ciardi, T. Macrì, and F. Cinti, Finite-temperature phases of trapped bosons in a two-dimensional quasiperiodic potential, Phys. Rev. A **105,** L011301 (2022).

[59] P. Jain, F. Cinti, and M. Boninsegni, Structure, Bose-Einstein condensation, and superfluidity of two-dimensional confined dipolar assemblies, Phys. Rev. B **84,** 014534 (2011).

[60] M. Boninsegni and N. V. Prokof'ev, Colloquium: Supersolids: What and where are they?, Rev. Mod. Phys. **84,** 759 (2012).

[61] A. J. Leggett, Can a solid be "superfluid?", Phys. Rev. Lett. **25,** 1543 (1970).

[62] P. Sindzingre, M. L. Klein, and D. M. Ceperley, Path-integral Monte Carlo study of low-temperature ^{4}He clusters, Phys. Rev. Lett. **63,** 1601 (1989).

[63] A. J. Moreno and C. N. Likos, Diffusion and relaxation dynamics in cluster crystals, Phys. Rev. Lett. **99,** 107801 (2007).

[64] The videos are available on request upon contacting the authors.

[65] Molecular dynamics particle trajectories for the harmonic trap (2023).

[66] Molecular dynamics particle trajectories for the icosahedral distribution of clusters (2023).

[67] L. Kaplan, N. T. Maitra, and E. J. Heller, Quantizing constrained systems, Phys. Rev. A **56,** 2592 (1997).

[68] P. Leboeuf and N. Pavloff, Bose-Einstein beams: Coherent propagation through a guide, Phys. Rev. A **64,** 033602 (2001).

[69] L. Salasnich, A. Parola, and L. Reatto, Effective wave equations for the dynamics of cigar-shaped and disk-shaped Bose condensates, Phys. Rev. A **65,** 043614 (2002).

[70] P. Sandin, M. Ögren, M. Gulliksson, J. Smyrnakis, M. Magiropoulos, and G. M. Kavoulakis, Dimensional reduction in Bose-Einstein condensed clouds of atoms confined in tight potentials of any geometry and any interaction strength, Phys. Rev. E **95,** 012142 (2017).

[71] L. Salasnich, Bose-Einstein condensate in an elliptical waveguide, SciPost Phys. Core **5,** 015 (2022).

[72] G.-H. Liang and M.-Y. Lai, Effective quantum dynamics in curved thin-layer system with inhomogeneous confinement, Phys. Rev. A **107,** 022213 (2023).

[73] H. Jensen and H. Koppe, Quantum mechanics with constraints, Ann. Phys. (N.Y.) **63,** 586 (1971).

[74] R. C. T. da Costa, Quantum mechanics of a constrained particle, Phys. Rev. A **23,** 1982 (1981).

[75] S. Prestipino, A. Laio, and E. Tosatti, Systematic improvement of classical nucleation theory, Phys. Rev. Lett. **108,** 225701 (2012).

[76] P. Hartman and A. Wintner, On the third fundamental form of a surface, Am. J. Math. **75,** 298 (1953).

[77] C. N. Likos, A. Lang, M. Watzlawek, and H. Löwen, Criterion for determining clustering versus reentrant melting behavior for bounded interaction potentials, Phys. Rev. E **63,** 031206 (2001).

[78] S. Prestipino and P. V. Giaquinta, Ground state of weakly repulsive soft-core bosons on a sphere, Phys. Rev. A **99,** 063619 (2019).

[79] T. Macrì, F. Maucher, F. Cinti, and T. Pohl, Elementary excitations of ultracold soft-core bosons across the superfluid-supersolid phase transition, Phys. Rev. A **87,** 061602(R) (2013).

[80] T. Macrì, S. Saccani, and F. Cinti, Ground state and excitation properties of soft-core bosons, J. Low Temp. Phys. **177,** 59 (2014).

[81] S. Franzini, L. Reatto, and D. Pini, Formation of cluster crystals in an ultra-soft potential model on a spherical surface, Soft Matter **14,** 8724 (2018).

[82] M. A. Baranov, Theoretical progress in many-body physics with ultracold dipolar gases, Phys. Rep. **464,** 71 (2008).

[83] We note that, despite this supersolid being quasi-one-dimensional, no supersolid phase exists in the strictly one-dimensional system; see, for instance, Ref. [84].

[84] T. Roscilde and M. Boninsegni, Off-diagonal correlations in a one-dimensional gas of dipolar bosons, New J. Phys. **12,** 033032 (2010).

[85] M. Sohmen, C. Politi, L. Klaus, L. Chomaz, M. J. Mark, M. A. Norcia, and F. Ferlaino, Birth, life, and death of a dipolar supersolid, Phys. Rev. Lett. **126,** 233401 (2021).

[86] J. Sánchez-Baena, C. Politi, F. Maucher, F. Ferlaino, and T. Pohl, Heating a dipolar quantum fluid into a solid, Nat. Commun. **14,** 1868 (2023).

[87] A. Recati and S. Stringari, Supersolidity in ultracold dipolar gases, Nat. Rev. Phys. **5,** 735 (2023).

[88] G. Li and D. K. Efimkin, Equatorial waves in rotating bubble-trapped superfluids, Phys. Rev. A **107,** 023319 (2023).

[89] C. Ryu, M. F. Andersen, P. Cladé, V. Natarajan, K. Helmerson, and W. D. Phillips, Observation of persistent flow of a Bose-Einstein condensate in a toroidal trap, Phys. Rev. Lett. **99,** 260401 (2007).

[90] L. Corman, L. Chomaz, T. Bienaimé, R. Desbuquois, C. Weitenberg, S. Nascimbène, J. Dalibard, and J. Beugnon, Quench-induced supercurrents in an annular Bose gas, Phys. Rev. Lett. **113,** 135302 (2014).

[91] Y. Guo, R. Dubessy, M. d. G. de Herve, A. Kumar, T. Badr, A. Perrin, L. Longchambon, and H. Perrin, Supersonic rotation of a superfluid: A long-lived dynamical ring, Phys. Rev. Lett. **124,** 025301 (2020).

SUPPLEMENTAL MATERIAL

This document contains additional information on the quantum simulation method, including a detailed description of our biased PIMC method. Some more details on classical simulations are also given. Finally, in the framework provided by the Gross-Pitaevskii equation, we discuss the changes intervening in the Hamiltonian of a loosely constrained interacting system when the original 3D description is reformulated in a lower-dimensional curved manifold.

Path integral Monte Carlo

The application of the Path integral Monte Carlo (PIMC) method to particles moving near the surface of a sphere has prompted us to develop a specialized version of PIMC that we illustrate in this section. For ease of understanding, we first recall the foundations of PIMC and its most common implementations, with a focus on the proposal and acceptance of new configurations.

Basically, PIMC relies on Feynman's path integral approach to the equilibrium statistical mechanics of quantum systems [49, 67, 68]. In this framework, all relevant information is contained in the canonical partition function, Z, which is the trace of the density matrix operator $e^{-\beta H}$, where H is the Hamiltonian and $\beta = (k_B T)^{-1}$. In the canonical ensemble, the partition function of N identical bosons reads:

$$Z = \frac{1}{N!} \sum_P \int d\mathbf{R}\, \rho(\mathbf{R}, P\mathbf{R}, \beta), \qquad (5)$$

where

$$\rho(\mathbf{R}, \mathbf{R}', \beta) = \langle \mathbf{R} | e^{-\beta H} | \mathbf{R}' \rangle \qquad (6)$$

is the density matrix and $P\mathbf{R} = (\mathbf{r}_{P(1)}, \mathbf{r}_{P(2)}, \ldots, \mathbf{r}_{P(N)})$ is a permutation of particle coordinates.

The path integral approach consists in breaking up β into M (imaginary-)time slices of length $\tau = \beta/M$, and rewriting the partition function as a convolution of density matrices (viz., imaginary-time propagators) at a higher temperature:

$$
\begin{aligned}
Z = \frac{1}{N!} \sum_P \int & d\mathbf{R}^0 d\mathbf{R}^1 \ldots d\mathbf{R}^{M-1} \\
& \times \rho(\mathbf{R}^0, \mathbf{R}^1, \tau) \rho(\mathbf{R}^1, \mathbf{R}^2, \tau) \cdots \rho(\mathbf{R}^{M-1}, P\mathbf{R}^0, \tau),
\end{aligned}
\qquad (7)
$$

where $\mathbf{R}^j = (\mathbf{r}_1^j, \mathbf{r}_2^j, \ldots, \mathbf{r}_N^j)$ is the vector of coordinates at a given time slice j. Therefore, associated with each particle i are M classical images $\mathbf{r}_i^j$ (also called beads), forming its imaginary-time trajectory (also called a polymer, path, or worldline). Using approximate forms for ρ at small τ, the thermodynamic properties of the quantum

system can be obtained by sampling suitable estimators on the Boltzmann distribution of a classical system of polymers, with the equivalence being exact in the limit $\tau \to 0$.

Worldline configurations can be sampled through a number of Monte Carlo schemes. The one we use, called the "worm algorithm", was developed in order to efficiently sample bosonic permutations; it works by opening the worldlines, allowing them to retract and extend in imaginary time [50], and, most importantly, to join with each other. This may lead to the formation of paths spanning a number of particles, which provides the visual representation of quantum coherence; sampling these paths properly is essential to correctly compute expectation values at low temperature.

Regardless of the scheme used, a crucial ingredient in the implementation of the PIMC method is the free-particle propagator. For simplicity, we specialize our discussion to the case of a single particle, but all concepts can be generalized to the many-particle case in a straight-forward way. In the absence of external and interaction potentials, the density matrix for a single particle reads:

$$\rho_{free}(\mathbf{r}, \mathbf{r}'; \tau) = \frac{1}{(4\pi\lambda\tau)^{d/2}} \exp\left\{ -\frac{(\mathbf{r} - \mathbf{r}')^2}{4\lambda\tau} \right\}, \qquad (8)$$

whereas, when potentials are present, in the limit $\tau \to 0$ it can be approximated as

$$\rho(\mathbf{r}, \mathbf{r}'; \tau) = \rho_{free}(\mathbf{r}, \mathbf{r}'; \tau)\, e^{-\tau V(\mathbf{r})}, \qquad (9)$$

called primitive approximation. In our simulations, we adopt this approximation to model the soft-core potential and the dipolar potential outside the core; the hard-core part of the latter is instead treated with the Cao-Berne propagator [69–71]. Convergence in τ is obtained for a number of timeslices between 64 and 256 in all cases. In a Monte Carlo scheme, new configurations are proposed by sampling a product of free-particle propagators and accepted or rejected based on the changes occurred in the external and interaction potentials. This is easily done computationally because the propagator (8) between two successive polymer beads has the form of a Gaussian distribution with variance $\sigma = \sqrt{2\lambda\tau}$, for which well-established sampling algorithms exist. In the context of the worm algorithm, which works with open worldlines, the simplest move is the propagation of the particle position from time slice j to the next one. The displacement of position $\mathbf{r}^{j+1}$ with respect to $\mathbf{r}^j$ is drawn from the distribution $\rho_{free}(\mathbf{r}^j, \mathbf{r}^{j+1}; \tau)$ and accepted or rejected depending on change in the potential, $V(\mathbf{r}^{j+1}) - V(\mathbf{r}^j)$. More generally, while updating the position of one bead at a time results in a slow simulation process, much more efficient moves are available: an essential ingredient of all PIMC algorithms are multilevel moves [68], which update an entire portion of worldline, open or closed, at once. Finally, moves that shift worldlines rigidly in space are also routinely employed.

More sophisticated techniques exist which, by relying on better approximations to the potential term, build upon the above procedure to improve the efficiency of the acceptance step. When it comes to the external potential, a special case is represented by the harmonic potential: in this case, an analytic solution is available for the full propagator

$$\rho_{osc}(\mathbf{r}, \mathbf{r}', \tau) = \langle \mathbf{r} | \exp \left\{ -\tau \frac{\hat{\mathbf{p}}^2}{2m} + \frac{m\omega^2 \hat{\mathbf{r}}^2}{2} \right\} | \mathbf{r}' \rangle , \quad (10)$$

requiring no separation between the kinetic and potential terms. In general, however, the external potential must be treated in the primitive approximation or through higher-order approximations [72]. As we now explain, this poses a problem for the bubble-trap potential, since, for $T \to 0$, it leads to reject almost every proposed configuration.

The size of a free particle — as well as the average diameter of the 3D polymer generated by sampling (8) — is proportional to the thermal wavelength, and therefore increases as the temperature is reduced, eventually becoming infinite when $T = 0$. It is immediate to realize that, no matter how the confining potential is chosen, most polymer beads will eventually lie in regions of space that are energetically unfavorable. To avoid this, it is necessary to work with a very large number of timeslices and displace only a few beads at a time, so that the displacements are on the same scale of the characteristic length associated with the external potential; clearly, this would make the simulation very slow. As we have seen, in the case of a harmonic potential this problem can be circumvented by using a harmonic propagator in place of the free-particle propagator. However, this would not hold for arbitrary confining potentials; for this reason, the use of PIMC is usually limited to free or harmonically confined interacting systems, or to bounded external potentials such as those featuring optical lattices [73].

Biased PIMC method for bubble traps

The biased PIMC algorithm proposed herein generates new configurations according to a distribution that is loosely tailored to fit the external potential. Compared to the standard algorithm, we introduce the following changes:

1) When attempting the propagation of a particle from time slice j to time slice $j + 1$, instead of generating the displacement from (8), we draw it from an anisotropic Gaussian distribution. A radial displacement is proposed with variance σ_r. An angular displacement is also proposed, derived from drawing a length from a two-dimensional Gaussian distribution with variance σ_θ. This length must then be converted into an angle; there are different ways to do this, so the specifics of the move can

vary, but this is not important since detailed balance will take care that small differences in the generated paths are smoothed out. For example, we can generate the length of arcs along the sphere; in this case, we draw l_θ from the Gaussian distribution and set $\theta = l_\theta / R$, leading to

$$P(\Delta r, \Delta \theta) = \frac{1}{\sqrt{2\pi}\sigma_r} e^{-\frac{\Delta_r^2}{2\sigma_r^2}} \frac{1}{2\pi\sigma_\theta^2} e^{-\frac{\Delta_\theta^2 R^2}{2\sigma_\theta^2}} . \quad (11)$$

Another option is that l_θ is the length of a chord, in which case $\theta = 2 \arcsin (l_\theta / 2R)$. We have tested both solutions and found no significant differences in the results.

2) In a multilevel move, we construct successive positions along an arc rather than along a straight line.

3) Instead of proposing rigid shifts of a worldline in 3D space, we make the move in two steps: a radial shift first and then a rotation of the worldline around the center of the sphere.

A move is drawn from a proposal kernel $T(R \to R')$, then accepted with probability $W(R \to R')$. In order for detailed balance to be satisfied, we adopt the Metropolis rule

$$W(R \to R') = \min \left\{ 1, \frac{T(R' \to R)}{T(R \to R')} \frac{\pi(R')}{\pi(R)} \right\} , \quad (12)$$

where π is the equilibrium distribution.

In the standard algorithm, $T(R \to R') \propto \rho_{free}(R')$, and since $\pi(R) \propto \rho_{free}(R')e^{-V(R')}$, the ρ_{free} terms will cancel out, leading to

$$W(R \to R') = \min \left\{ 1, \frac{e^{-V(R')}}{e^{-V(R)}} \right\} . \quad (13)$$

In the biased algorithm, $T(R \to R')$ is a different distribution and all terms in (12) must be computed explicitly. This may cause issues when σ_r or σ_θ are very different from $\sqrt{2\lambda\tau}$, because large terms in the fraction can lead to either very large or very small acceptance rates depending on the move, especially in the worm algorithm when beads are removed altogether. For this reason, we employ symmetric moves where, whenever a worldline segment is deleted, it is immediately replaced by a new one. It is also possible to simulate the limiting case where $u_0 \to \infty$ by simply setting $\sigma_r = 0$. The above procedure is applied for both closed worldline configurations and "worm moves" involving open worldlines. As an illustrative example, in Fig. 6 we show the worldline configuration at a single simulation step in equilibrium, corresponding to the cluster supersolid in Fig. 1b.

To confirm that bosons are confined near the spherical surface, we look at the radial density profile, which is the particle density integrated over the solid angle. In Fig. 7, we show the radial density at three values of λ, corresponding to the three cases of Fig. 1. Indeed, we see that particles are lying near the spherical surface, as expected from the implementation of our biased PIMC
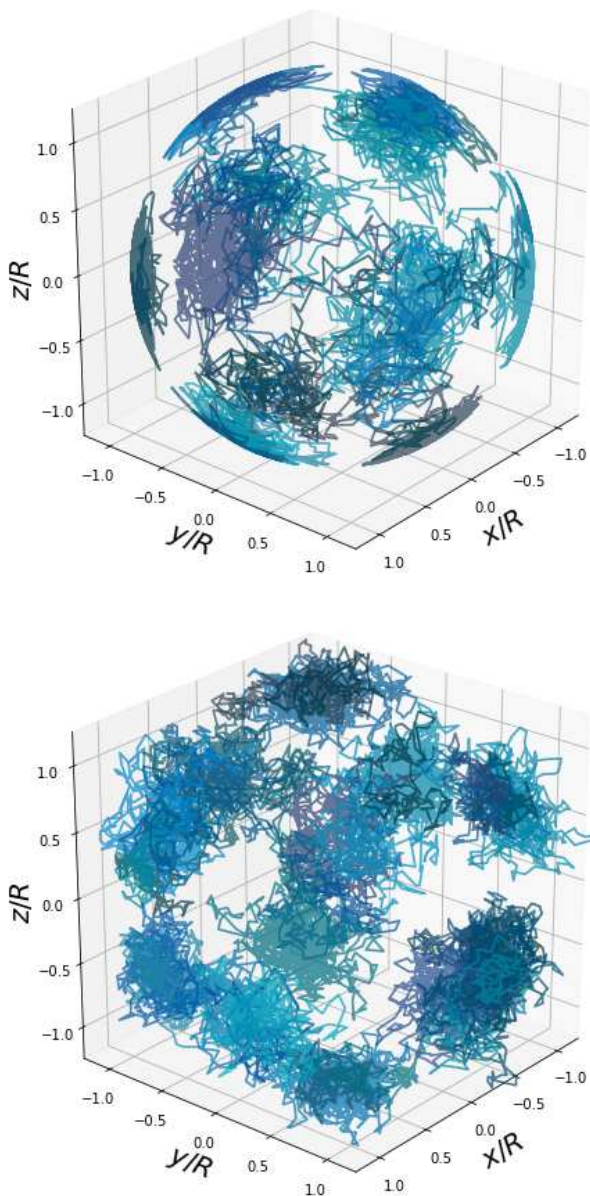
Figure 7. Radial density profile at $N = 120, T = 0.125, R = 1.4$, and $\lambda = 0.5$ (blue dotted line), 0.16 (blue dashed line), 0.01 (purple solid line). Here $u_0 = 2$.
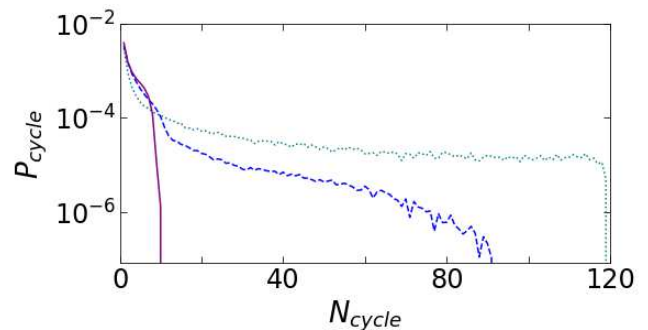
Figure 8. Relative frequency with which permutation cycles of various lengths occur at $N = 120, T = 0.125, R = 1.4$, and $\lambda = 0.5$ (blue dotted line), 0.16 (blue dashed line), 0.01 (purple solid line). Here $u_0 = 2$.

Figure 6. Snapshot of a typical configuration of the soft-core system in the polymer representation at $T = 0.5$, $R = 1.4$, and $\lambda = 0.16$. Each of the worldlines consists of $M = 64$ beads. The shades of blue distinguish between distinct groups of connected worldlines. Top: $u_0 = \infty$. Bottom: $u_0 = 2$. In either case the number of clusters is 12.

for bubble traps. Interestingly, when the effects of delocalization are important (superfluid phase at $\lambda = 0.5$, cyan dotted line; and supersolid phase at $\lambda = 0.16$, blue dashed line), the distributions appear broader than in the other case of the normal cluster solid ($\lambda = 0.01$, purple solid line), which instead displays a sharper peak.

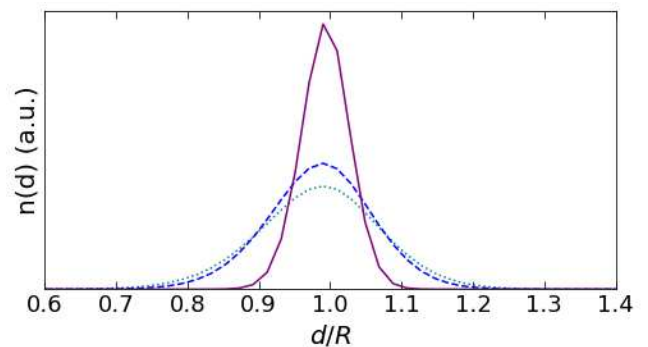A key point to explore the effects of quantum statistics through a PIMC simulation is the distribution of polymer lengths, which is intrinsically connected to the indistinguishability of the particles and reflects quantum coherence as well as delocalization [74]. In this framework, we consider the probability P_{cycle} to find polymer chains involving N_{cycle} particles, which we call permutation cycles ($1 \leq N_{\text{cycle}} \leq N$). This probability is obtained by updating at each step a histogram of N_{cycle}. Fig. 8 reports results for the same set of parameters in Fig. 1a-c. In the superfluid regime ($\lambda = 0.5$, cyan dotted line) we find permutations extending over groups of particles of any number of particles. As the kinetic term decreases ($\lambda = 0.16$, blue dashed line), the system enters a supersolid regime where we still observe permutation cycles over a considerably large amount of particles, again implying global coherence among clusters. Finally, for small λ values ($\lambda = 0.01$, purple solid line) permutations only involve the bosons contained in the same cluster. Here we have a normal solid phase, where quantum effects are limited to the single droplet.

Superfluidity and area estimator

A strong point of the PIMC method is the possibility to identify a phase with a periodic modulated density as supersolid [75]. Indeed, a characteristic feature of supersolids is their response to a slow axial rotation [76], which occurs with a reduced moment of inertia relative to an ordinary solid of same mass. The superfluid fraction f_s, i.e., the relative reduction in the moment of inertia, can be accurately estimated in a PIMC simulation.

In bubble traps, f_s has been evaluated by sampling the so-called "area estimator" [77]. This method draws a direct connection between the area enclosed by tangled paths of polymers in a finite system and the reduction of the moment of inertia of the particles compared to the classical case. For reasons of symmetry, we only inspect the superfluid fraction along three orthogonal axes ($k = x$, y, and z). When doing so, the formula for $f_s^{(k)}$ reads:

$$f_s^{(k)} = \frac{4m^2}{\hbar^2} \beta I_{cl}^{(k)} \left(\langle A_k^2 \rangle - \langle A_k \rangle^2 \right) , \qquad (14)$$

where we keep the full definition by Sindzingre *et al.* in Ref. [73, 77]. In this formula, A_k is the total area enclosed by particle paths projected onto the plane perpendicular to axis k, which can be written in terms of particle positions as

$$A_k = \frac{1}{2} \sum_{i=1}^{N} \sum_{j=0}^{M-1} \left(\mathbf{r}_i^j \times \mathbf{r}_i^{j+1} \right)_k , \qquad (15)$$

whereas $I_{cl}^{(k)}$ is the classical moment of inertia around the k axis.

For the isotropic soft-core fluid, the superfluid fraction along any of the principal directions is the same within errors; therefore, we only report data for $f_s = (f_s^x + f_s^y + f_s^z)/3$. Conversely, in the dipolar case the anisotropy of the interaction makes it so that f_s^z differs from f_s^x and f_s^y over a significant range of parameters; therefore, in figures their values are reported separately.

The pair distribution function

For clarity, here we describe the method of computing the pair distribution function, whose formal definition as a thermal average is (for spinless particles):

$$g(r) = \rho^{-2} \langle \Psi^\dagger(\mathbf{x}) \Psi^\dagger(\mathbf{x}') \Psi(\mathbf{x}') \Psi(\mathbf{x}) \rangle \qquad (16)$$

where $r = |\mathbf{x} - \mathbf{x}'|$ is the Euclidean distance in three dimensions, ρ is the number density, and Ψ and $\Psi^\dagger$ are field operators (an average over the direction of $\mathbf{x} - \mathbf{x}'$ is implied in (16)). In a PIMC simulation, $g(r)$ is sampled as a histogram. The interparticle distance r is divided into bins, and a reference particle is chosen; at each
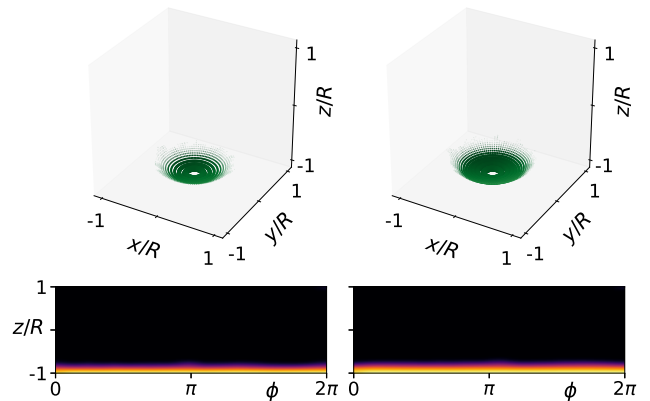

Figure 9. Non-interacting bosons (left) and bosons with hard-core interaction, $a = 50 \, a_0$ (right) in the presence of gravity. In both cases, as expected, particles fall to the bottom of the trap.

sampling step, the distance between the reference particle and each other particle is calculated, and the value of the corresponding bin in the histogram is increased. The resulting histogram is then averaged over sampling steps. In Euclidean three-dimensional space, normalization is accomplished by dividing by a factor of $4\pi r^2$; in the present case, a number of different choices could be made, but we decide to keep the same normalization. In a PIMC simulation, sampling is done at each time slice and further averaged over time slices.

Simulations with gravity

We have performed simulations in the presence of a gravitational field with $g = 9.81 \, \mathrm{m/s^2}$. In Fig 9, we show results for the non-interacting and hard-core cases, confirming that the simulations give the expected result of particles sagging to the bottom of the bubble trap.

Classical simulations

We herein present, with more detail than provided in the main text, the results of Monte Carlo (MC) and molecular dynamics (MD) simulations of classical penetrable spheres of diameter σ, subject to the external potential in Eq. (2). For simplicity, in MD simulations we actually employ a continuous generalized exponential model potential with exponent 30, which would have practically the same behavior of the penetrable-sphere model. Simulations are performed at fixed $N = 120, T = 0.5, u_0 = 2$, and $\Omega = 0.0441$, while the reference radius R is varied through Δ.

We employ the standard Metropolis MC algorithm with local and non-local moves. At each MC step, after

randomly selecting a particle i with position $\mathbf{r}_i$ and distance $d_i = |\mathbf{r}_i|$ from the trap center, a move is attempted from $\mathbf{r}_i$ to $\mathbf{r}'_i$, choosing between two equally likely possibilities: 1) $\mathbf{r}'_i$ is drawn at random from a cube of side 2δ centered at $\mathbf{r}_i$; 2) $\mathbf{r}'_i$ is an arbitrary point on the sphere of radius d_i. As usual, δ is adjusted during the equilibration stage so as to ensure an average 40-50% acceptance of type-1 moves. In MD simulations, the timestep is $dt = 0.005\sqrt{\frac{m\sigma^2}{\epsilon}}$, where m is the mass of the particles, and the thermal bath is modeled by a Nosé-Hoover thermostat with a temperature damping factor $\tau = 100\, dt$ in time units. As for the initial configuration, we consider two possibilities: either the particles are placed at random on the reference sphere, or they are homogeneously distributed inside it (except for the case of the harmonic trap, where they are all placed at $R = 0$). We generate hundreds of million MC steps and let the system evolve for a similar number of MD timesteps, to reduce the chance that the system might remain trapped in a metastable state. In the case of MD simulations, the initial velocities are randomly selected according to a Gaussian distribution. For R less than 1.5, the system invariably relaxes to a clustered configuration. Once a stable cluster phase has formed, jump diffusion events [78] between the clusters are extremely rare on the time scale of the simulations. As a function of R, we observe a sequence of "transitions" between different cluster arrangements ("phases"), which in MC simulations are all characterized by equally populated clusters, until the spherical density becomes so small that a homogeneous fluid is formed.

R	classical	quantum ($\lambda = 0.16$)
0	5 (3+2), 7 (5+2)	6 (OCT)
0.21	6 (OCT), 7 (5+2)	
0.42	4 (TET), 5 (3+2), 8 (SAP)	6 (OCT)
0.63	4 (TET)	
0.84	6 (OCT)	6 (OCT)
1.05	10 (SAP+2)	
1.155	12 (ICO)	8 (SAP)
1.26	15	
1.4	20	12 (ICO)

Table I. Number N_c of clusters and their spatial arrangement as a function of R (see text). The list of abbreviations is as follows. 4 (TET): 4 equivalent clusters at the vertices of a regular tetrahedron (TET). 5 (3+2): 3 clusters at the vertices of an equilateral triangle + 2 clusters on the axis of the triangle, farther from the origin. 6 (OCT): 6 equivalent clusters at the vertices of a regular octahedron (OCT). 7 (5+2): 5 clusters at the vertices of a regular pentagon + 2 clusters on the axis of the pentagon, closer to the origin. 10 (SAP+2): 8 equivalent clusters at the vertices of a square antiprism (SAP) with regular faces + 2 clusters on the axis of the antiprism, at the same distance from the origin. 12 (ICO): 12 equivalent clusters at the vertices of a regular icosahedron (ICO).

We report in Table 1 the final number N_c of clusters and their overall arrangement for a few R values, including for comparison also the available results of quantum simulations for $\lambda = 0.16$. For the smaller R values, two or three values of N_c are quoted in the table, since the outcome of simulation showed a dependence on the simulation method and/or the initial configuration, suggesting the existence of several long-lived states that are close in free energy and are protected by high free-energy barriers. Similar problems exist in quantum simulations for small values of λ and R. As a rule, relaxation to equilibrium is faster the larger is R.

To demonstrate the difference in relaxation time between small and large R values, we have prepared two MD movies [79]. In the first movie [80], we show four segments from a MD simulation 5×10^8 timesteps long, for the case $R = 0$ (harmonic trap). Each segment of simulation lasts 5000 timesteps and particle configurations are dumped every 10 timesteps, corresponding to 500 video frames. In the first segment, starting from $t = 0$, we monitor the onset of a large cluster at the origin along with a few satellites made up of a single particle each. Following this event, for several hundreds of thousand MD timesteps we observe a system of four clusters, where the largest cluster still lies near the origin, while the remaining three clusters continue to grow. Only in the last few million MD steps, we observe the formation of a fifth cluster, initially consisting of a single particle, and we report this event in the second segment of the movie. In the third segment, we show the addition of a new particle to the fifth cluster, whereas in the last segment the addition of another particle makes the cluster finally populated with three particles. Our reasonable guess about the future evolution of the system is that the growth of the less-populated clusters will continue until the number of particles in all five clusters becomes nearly equal. In the second movie [81], relative to $R = 1.155$, we follow the simulation for 5000 timesteps, starting from $t = 0$, with particle configurations still dumped every 10 timesteps. Starting from an initial configuration where particles are randomly distributed over the spherical surface, we monitor the quick formation of eleven clusters in the first hundred timesteps. Then, after approximately $3 - 4$ seconds of movie (about 1000 timesteps), we see one of the clusters stretching and eventually breaking in two distinct clusters, thus giving rise to the stable icosahedral configuration referred to in Table 1. In summary, in the case of the harmonic trap ($R = 0$), after $5 \times 10^8 dt$ a structure with five clusters is established, but many more steps are likely needed in order that clusters become equally populated. On the contrary, for $R = 1.155$, the approach to equilibrium is extremely fast: it only takes about $10^3 dt$ for the clusters to assemble in an icosahedral arrangement.

We further illustrate the features of cluster phases by reporting in Fig. 10 results for two structural functions: the pair distribution function $g(r)$, r being the Euclidean
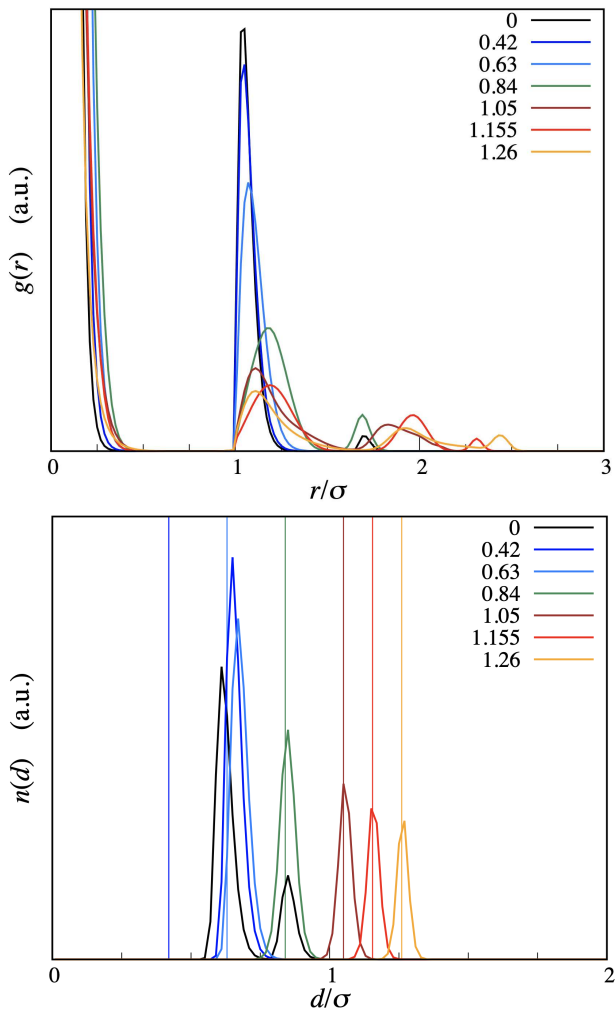
Figure 10. Top: pair distribution function. Bottom: radial density. In the bottom panel, the vertical lines mark the various R values. The only case where $n(d)$ shows two peaks is $R = 0$ ($N_c = 5$). Observe that for $R = 0.42$ ($N_c = 4$) the average distance of clusters from the origin is rather different from R. Also notice that $N_c = 10$ for the $R = 1.05$ case shown here.

distance of a particle from a reference particle, and the radial density $n(d)$, where d denotes the distance of a particle from the trap center. As R grows, the transitions between different "phases" are reflected in qualitative changes of $g(r)$. The profile of $n(d)$ also changes, from one characterized by two peaks at $R = 0$ to a single progressively sharper peak for $R > 0$. For not too small radii, the rationale behind the choice of the equilibrium arrangement seems to be providing clusters with the most efficient occupation of the available space or, equivalently, with the highest coordination number Z. Due to geometric frustration, i.e., to the obstruction of triangular order due to curvature, this number cannot

be six. As R varies, the system adjusts the number of clusters so as to keep the distance between neighboring droplets always close to ≈ 1.25 (see top panel of Fig. 10); in turn, this implies an increase of Z with R towards the asymptotic value of 6.

Thin-shell limit

The quantization of a system of particles confined to a curved surface raises formidable challenges that can be pragmatically solved by regarding the constraint as the limit of a large restoring force arising when the particle coordinates deviate from their constrained values [82]. Atoms in a bubble trap provide a perfect representation of this viewpoint, as confinement to a spherical surface is here realized through an external potential that becomes progressively tighter as the radius R of the reference sphere $\mathscr{S}$ increases. When R is large enough the external potential reduces to a narrow harmonic well that constrains particles in the immediate neighborhood of the $\mathscr{S}$ surface. The question then arises as to what two-dimensional (2D) description is better suited to represent such a strong confinement. While simulation results remain the ultimate benchmark for the accuracy of any theoretical proposal, some clues on the nature of the reduced description are provided by zero-temperature calculations. Dimensional reduction at the level of the Gross-Pitaevskii (GP) equation has been considered in various papers: depending on the geometry of the trap, both one-dimensional (1D) [83–86] and 2D effective descriptions [17, 87] can arise, where additional terms appear in the GP equation as a result of a strong (though not infinitely strong) confining field. Specifically, common to all such approaches is that the motion of quantum particles constrained to a curved surface is affected by a curvature-induced geometric potential [88, 89]. By elaborating further on the treatment put forth in [17], we sketch below the derivation of the generalized GP equation for an arbitrary interaction between the particles, and then specialize our discussion to the spherical surface.

Let Σ be a regular surface and call $\mathbf{R}(u, v)$ the parametrization of a small piece of Σ ("patch"). For points $\mathbf{r}$ close to this portion of Σ, it is convenient to switch from Cartesian coordinates, $\mathbf{r} = (x, y, z)$, to new coordinates $q^i = (u, v, \zeta)$ (parallel and orthogonal to Σ), see e.g. Ref. [90]:

$$\mathbf{r} = \mathbf{R}(u, v) + \zeta \hat{\mathbf{n}}(u, v), \qquad (17)$$

where

$$\hat{\mathbf{n}}(u, v) = \frac{\mathbf{R}_u \wedge \mathbf{R}_v}{|\mathbf{R}_u \wedge \mathbf{R}_v|} \qquad (18)$$

is the unit normal to Σ. Transformation (17) is one-to-one sufficiently close to Σ. We will later consider the limit

where the patch deviates only slightly from planarity, meaning that the local radii of curvature are much larger than the maximum allowed value of $|\zeta|$. Moreover, we denote $\Sigma(\zeta)$ the 2D manifold ("parallel" to Σ) obtained by shifting all points of Σ by ζ along the normal direction.

The metric tensor G_{ij} (with $i, j = 1, 2, 3$) relative to the transformation (17) reads:

$$G_{ij} \equiv \frac{\partial \mathbf{r}}{\partial q^i} \cdot \frac{\partial \mathbf{r}}{\partial q^j} = \begin{pmatrix} g_{uu} & g_{uv} & 0 \\ g_{vu} & g_{vv} & 0 \\ 0 & 0 & 1 \end{pmatrix} \qquad (19)$$

with

$$\begin{aligned} g_{\alpha\beta} &= \mathbf{R}_\alpha \cdot \mathbf{R}_\beta + 2\mathbf{R}_\alpha \cdot \frac{\partial \hat{\mathbf{n}}}{\partial q^\beta} \zeta + \frac{\partial \hat{\mathbf{n}}}{\partial q^\alpha} \cdot \frac{\partial \hat{\mathbf{n}}}{\partial q^\beta} \zeta^2 \\ &\equiv g_{\alpha\beta}^{(0)} + 2 s_{\alpha\beta} \zeta + h_{\alpha\beta} \zeta^2 \quad \text{(for } \alpha, \beta = 1, 2\text{)} \,. \end{aligned} \qquad (20)$$

In differential geometry, $g_{\alpha\beta}^{(0)}$ and $s_{\alpha\beta}$ are respectively known as the first and second fundamental forms of Σ. The third fundamental form, $h_{\alpha\beta}$, is related to the previous two by [91]

$$h_{\alpha\beta} = -K g_{\alpha\beta}^{(0)} + 2 H s_{\alpha\beta} \,, \qquad (21)$$

H and K being the mean and Gaussian curvature of Σ, respectively.

As usual (see, e.g., Ref. [53]), the GP equation is derived by extremizing the grand potential per unit volume at $T = 0$, $\omega[\psi]$, written as a functional of a trial condensate wave function ψ:

$$\begin{aligned} \omega[\psi] &= \rho \int_{\mathscr{N}} \mathrm{d}^3 r \, \psi^*(\mathbf{r}) \left[-\frac{\hbar^2}{2m} \nabla^2 + V_{\text{ext}} \right. \\ &\left. + \frac{N-1}{2} \int_{\mathscr{N}} \mathrm{d}^3 r' \, u(|\mathbf{r} - \mathbf{r}'|) |\psi(\mathbf{r}')|^2 - \mu \right] \psi(\mathbf{r}) \,, \end{aligned} \qquad (22)$$

where $V_{\text{ext}}(\mathbf{r})$ is the confining field and $\mathscr{N}$ is the neighborhood of Σ where particles are forced to lie. In order to separate the tangential from the normal motion, the above integral should first be written in terms of (u, v, ζ) coordinates (for each single patch of Σ). Then, the idea is to integrate out the ζ dependence everywhere, so as to remain with a functional of the 2D wave function only. After the change of coordinates, the kinetic-energy operator is still $-\hbar^2/(2m)$ times the Laplacian, for so it is prescribed by canonical quantization. Now, in curvilinear coordinates the Laplacian operator is given by

$$\nabla^2 = \frac{1}{\sqrt{\det G}} \frac{\partial}{\partial q^i} \left(\sqrt{\det G} \, G^{ij} \frac{\partial}{\partial q^j} \right) , \qquad (23)$$

as it follows from the Voss-Weyl formula for the divergence operator. Since $\det G = \det g$ and $G^{3j} = \delta_{j,3}$, we immediately find:

$$\nabla^2 = \nabla_\zeta^2 + \frac{\partial \ln \sqrt{\det g}}{\partial \zeta} \frac{\partial}{\partial \zeta} + \frac{\partial^2}{\partial \zeta^2} \,, \qquad (24)$$

where

$$\nabla_\zeta^2 = \frac{1}{\sqrt{\det g}} \frac{\partial}{\partial q^\alpha} \left(\sqrt{\det g} \, g^{\alpha\beta} \frac{\partial}{\partial q^\beta} \right) \qquad (25)$$

is the Laplacian restricted to $\Sigma(\zeta)$.

Following the suggestion of [17] we write the wave function of the condensate as

$$\psi(u, v, \zeta) = \frac{1}{\sqrt[4]{2\pi\sigma^2}} e^{-\frac{\zeta^2}{4\sigma^2}} \frac{\phi(u, v)}{\sqrt[4]{\det g}} \,, \qquad (26)$$

where σ (not to be confused with a particle diameter) is a small variational parameter and $\psi_r(u, v) = \phi(u, v) / \sqrt[4]{\det g^{(0)}}$ represents the 2D wave function of the system. The Gaussian function in Eq. (26) plays the role of system ground state along the normal direction, where the confining field acts as a harmonic potential:

$$V_{\text{ext}}(\zeta) = \frac{1}{2} m \omega^2 \zeta^2 \,. \qquad (27)$$

Assuming that the thickness $\sqrt{\hbar/(m\omega)}$ of $\mathscr{N}$ is much smaller than the minimum radius of curvature of the patch, the normalization of (26) should be effectively read as

$$1 = \int \mathrm{d}u \, \mathrm{d}v \, |\phi(u, v)|^2 = \int \mathrm{d}u \, \mathrm{d}v \, \sqrt{\det g^{(0)}} |\psi_r(u, v)|^2 \,. \qquad (28)$$

It is now straightforward, even though lengthy, to calculate the Laplacian (24) of the ψ function in (26):

$$\begin{aligned} \nabla^2 \psi &= \left\{ \left[\frac{\zeta^2}{4\sigma^4} - \frac{1}{2\sigma^2} - \frac{1}{4} \left(\frac{\partial \ln \sqrt{\det g}}{\partial \zeta} \right)^2 \right. \right. \\ &\left. - \frac{1}{2} \frac{\partial^2 \ln \sqrt{\det g}}{\partial \zeta^2} - \frac{\zeta}{2\sigma^2} \frac{\partial \ln \sqrt{\det g}}{\partial \zeta} \right] \frac{\phi(u, v)}{\sqrt[4]{\det g}} \\ &\left. + \nabla_\zeta^2 \frac{\phi(u, v)}{\sqrt[4]{\det g}} \right\} \frac{e^{-\frac{\zeta^2}{4\sigma^2}}}{\sqrt[4]{2\pi\sigma^2}} \,. \end{aligned} \qquad (29)$$

The next step is to approximate the first and second derivatives of $\ln \sqrt{\det g}$ by their $\zeta = 0$ values, and similarly replace the restricted Laplacian term with $\nabla_0^2 \psi_r$, so that decoupling of coordinates becomes possible. A similar procedure yields for the interaction term:

$$\begin{aligned} &\int_{\mathscr{N}} \mathrm{d}^3 r \, \psi^*(\mathbf{r}) \int_{\mathscr{N}} \mathrm{d}^3 r' \, u(|\mathbf{r} - \mathbf{r}'|) |\psi(\mathbf{r}')|^2 \psi(\mathbf{r}) \\ &= \int \mathrm{d}u \, \mathrm{d}v \, \sqrt{\det g^{(0)}(u, v)} |\psi_r(u, v)|^2 \\ &\quad \times \int \mathrm{d}u' \mathrm{d}v' \sqrt{\det g^{(0)}(u', v')} \\ &\quad \times \int \mathrm{d}\zeta \mathrm{d}\zeta' \, u(|\mathbf{r} - \mathbf{r}'|) \frac{1}{2\pi\sigma^2} e^{-\frac{\zeta^2 + \zeta'^2}{2\sigma^2}} |\psi_r(u', v')|^2 \,. \end{aligned} \qquad (30)$$

The inner integral above is computed at the lowest order in σ, obtaining:

$$\int \mathrm{d}\zeta \mathrm{d}\zeta' \, u(|\mathbf{r} - \mathbf{r}'|) \frac{1}{2\pi\sigma^2} e^{-\frac{\zeta^2 + \zeta'^2}{2\sigma^2}} = w(\mathbf{R} - \mathbf{R}', \hat{\mathbf{n}}, \hat{\mathbf{n}}') \,, \tag{31}$$

where

$$w(\mathbf{x}, \hat{\mathbf{n}}, \hat{\mathbf{n}}') = u(x) + \sigma^2 \left\{ \frac{u'(x)}{x} \right. $$
$$- \frac{1}{2} \left[(\hat{\mathbf{n}} \cdot \hat{\mathbf{x}})^2 + (\hat{\mathbf{n}}' \cdot \hat{\mathbf{x}})^2 \right] \left(\frac{u'(x)}{x} - u''(x) \right) \right\}$$
$$+ \mathscr{O}(\sigma^4) \,. \tag{32}$$

Hence, the curvature modifies the interaction between two particles, which acquires an additional dependence of order σ^2 on the normal vectors at the positions of the particles.

In conclusion, the grand potential becomes a functional of ψ_r:

$$\omega[\psi_r] \approx \rho \int \mathrm{d}u \, \mathrm{d}v \sqrt{\det g^{(0)}} \psi_r^*(u, v) \left\{ -\frac{\hbar^2}{2m} \nabla_0^2 \right.$$
$$+ \frac{\hbar^2}{4m} \left[\frac{1}{2} \left(\frac{\partial \ln \sqrt{\det g}}{\partial \zeta} \right)^2 + \frac{\partial^2 \ln \sqrt{\det g}}{\partial \zeta^2} \right]_{\zeta=0}$$
$$+ \frac{\hbar^2}{8m\sigma^2} + \frac{1}{2}m\omega^2\sigma^2 + \frac{N-1}{2}$$
$$\times \int \mathrm{d}u' \mathrm{d}v' \sqrt{\det g^{(0)\prime}} \, w(\mathbf{R} - \mathbf{R}', \hat{\mathbf{n}}, \hat{\mathbf{n}}') |\psi_r(u', v')|^2$$
$$- \left. \mu \right\} \psi_r(u, v) \,. \tag{33}$$

Upon imposing that the functional derivative of $\omega[\psi_r]$ with respect to ψ_r^* is zero, we arrive at the GP equation in reduced dimensionality:

$$\mu\psi_r = \left(-\frac{\hbar^2}{2m} \nabla_0^2 + V_{\mathrm{q}} + \frac{\hbar^2}{8m\sigma^2} + \frac{1}{2}m\omega^2\sigma^2 + (N-1) \right.$$
$$\times \left. \int \mathrm{d}u' \, \mathrm{d}v' \sqrt{\det g^{(0)\prime}} \, w(\mathbf{R} - \mathbf{R}', \hat{\mathbf{n}}, \hat{\mathbf{n}}') |\psi_r(u', v')|^2 \right) \psi_r \,, \tag{34}$$

where

$$V_{\mathrm{q}}(u, v) = \frac{\hbar^2}{4m} \left[\frac{1}{2} \left(\frac{\partial \ln \sqrt{\det g}}{\partial \zeta} \right)^2 + \frac{\partial^2 \ln \sqrt{\det g}}{\partial \zeta^2} \right]_{\zeta=0} \tag{35}$$

is the *geometric potential* [88, 89] and σ is to be adjusted so that the functional derivative of (33) with respect to σ vanishes too (the optimal σ would be of the order of $\sqrt{\hbar/(m\omega)}$). Clearly, Eq. (34) resembles the standard GP equation, except for three additions: 1) a constant energy shift; 2) a $\mathscr{O}(\sigma^2)$ correction to the interaction between two particles; and 3) a curvature-induced external field V_{q}.

For the spherical surface of radius R, the natural coordinates are the spherical angles θ and ϕ. Then, $g_{\theta\theta}^{(0)} = R^2, g_{\theta\phi}^{(0)} = g_{\phi\theta}^{(0)} = 0, g_{\phi\phi}^{(0)} = R^2 \sin^2 \theta$, while $H = 1/R$ and $K = 1/R^2$. Using the general formula [17]

$$\det g = \det g^{(0)} (1 + 4H\zeta + (4H^2 + 2K)\zeta^2 + 4HK\zeta^3 + K^2\zeta^4) \,, \tag{36}$$

we obtain

$$\det g = R^4 \sin^2 \theta \left(1 + \frac{\zeta}{R} \right)^4 \,. \tag{37}$$

It then follows from the latter equation that the geometric potential (35) is identically zero for the spherical surface [17].